9

Engineering Particle Agglomerate and Flame Propagation in 3D-printed Al/CuO Nanocomposites

Haiyang Wang and Michael R. Zachariah

University of California, Department of Chemical and Environmental Engineering, Riverside, CA 92521, USA

9.1 Introduction

Because of high combustion enthalpy (such as with oxygen) and availability, conventional aluminum microparticles (Al MPs) are commonly used in solid rocket propellant and other propulsive systems [1–3]. Although the total energy density of the system is increased after the addition of Al MPs, the burning rate was not found to improve much, resulting in a low energy release rate [4]. Additionally, Al MPs have a high ignition temperature of $\sim$2300 K, delaying the ignition of the system [2, 5, 6]. Luckily, the use of Al NPs lower the ignition temperature to <1000 K, with an enhanced burning rate and a lower ignition delay time [6–12]. Typically, as shown in Figure 9.1, Al MPs-based propellants have a stand-off flame zone (Figure 9.1a), due to the high ignition temperature and delay time of Al MPs, whereas the Al NPs-based propellant surface has a short- stand-off and much smaller burning particles [13]. Therefore, for Al MPs burning, most of the heat release occurs far from the burning surface, which provides weak heat feedback. In contrast, the heat feedback is enhanced with Al NPs as they are burning on or near the propellant surface. Typically, the maximum increase is by a factor of two when replacing Al MPs with NPs in solid propellants.

Another issue in the utilization of nanomaterials is the particle loading limitations in the fabrication of polymer nanocomposites. While high particulate loading can be found in polymer composites these systems involve relatively large super-micron particles [14]. Nanometallic fuels in contrast have been limited by significant processing challenges because the integration of nanoparticles into polymers significantly increases viscosity, making traditional casting methods unfeasible as well as limiting additive manufacturing approaches. As such nanothermites have found limited implementation because particle loadings are not sufficient to obtain high energy densities [5, 15–17]. One approach to resolve the increased viscosity is to assemble these nanoparticles into microspheres while retaining their nanoscale features [15, 16, 18, 19]. Recently, there has been an emerging interest in using additive manufacturing methods to prepare structural energetic materials

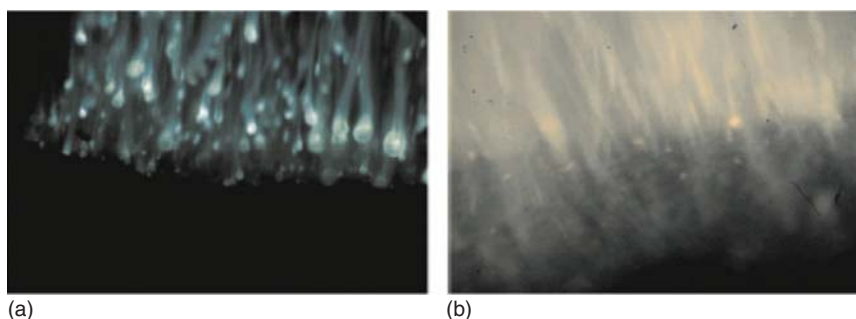(a)   (b)

Figure 9.1 Different burning surfaces for solid propellant at 1 MPa with Al MPs (a) and NPs (b). Al MPs are 30 μm spheres in HTPB at 10 bar and Al NPs are 100 nm spheres in polypropylene glycol (PPG) at 10 bar. Source: DeLuca [13], Reproduced with permission from Elsevier.

via templating [20], melting-extruding [21], inkjet printing [22], electrophoretic deposition [23], photopolymerization [14], foaming [24], and more. Among the many methods, direct writing of solvent-based inks is of particularly high interest due to its relative simplicity and convenience [25–28], moreover, the safety of the energetic materials can be dramatically enhanced when processed with a solvent. In a common ink, polymeric binders are used to provide structural integrity to the energetic formulations and afford mechanically stable, relatively insensitive, machinable, and formable energetic architectures. Since binders are generally non-energetic, it is preferred that the binder be added in the minimum quantity necessary to maintain the desired mechanical properties. In the last few decades, hydroxyl-terminated polybutadiene (HTPB) has found common use as the binder in the solid propellant, however, the curing time is too long (days) to be used for the direct-writing approach [29–31]. New binders or binder hybrids are desired to achieve high particle loading and high energy density.

Nanothermites are a class of energetic material with fuel (such as Al) and oxidizer (CuO, Fe_2O_3, MoO_3, Bi_2O_3, etc.) being mixed at the nanoscale, which undergoes a rapid redox reaction upon ignition [32]. Compared to conventional CHNO explosives such as TNT, RDX, and HMX, energetic nanocomposites such as nanothermites are attracting more attention for their high enthalpy of reaction and adjustable reactivity [33–39]. Their high surface area gives them a substantially higher energy release rate in comparison to their micron counterparts, thus making them potential candidates for materials whose reactivity falls in-between primary explosives and conventional pyrotechnics. This unique category, which has both military and civilian applications, such as gas generators [40, 41], nanoscale welding [42, 43], micropropulsion [44, 45], ammunition primers [46], and electric igniters [47, 48], as well as energetic additives in explosives and propellants [46, 49, 50]. However, their implementation is limited due to the inherent complexity of heterogeneous combustion that has yet to be fully understood. For example, theoretically, when reducing the size of the composition constituents to the nanoscale, the energy release rate should be enhanced by orders of magnitudes due to a highly increased

interfacial area and reduced diffusion distance between fuel and oxidizer [51–53], however, they have yet to exhibit such impressive enhancements [54–56]. One of the major concerns that may explain this underwhelming enhancement is the loss of nanostructure during the reaction, i.e. agglomeration or sintering.

Agglomeration, or sintering, is an important component in the combustion of Al NPs based energetics, which plays a significant role by rapidly melting and coalescing aggregated Al NPs and increasing the initial size of the reacting composite powders before burning (sintering time ≤ reaction time) [56]. Reactive molecular dynamics simulation has found that the sintering behavior may be enhanced by an induced built-in electric field between the metal and native oxide coating resulting in a softening of the alumina coating [57]. Agglomeration of aluminum (Al) particles has been commonly observed in solid propellants, which leads to losses in specific impulse (two-phase loss) and ultimately balances out any potential advantages of Al addition [58–60]. Using capture/quench studies, the agglomerate size of Al has been related to the burn rate of solid propellants and various approaches have been explored to efficiently reduce the effect of agglomerations [61–63]. In addition to ex situ studies, recently developed techniques such as time-resolved X-ray imaging [64, 65], and digital in-line holography [59, 60] have been employed to observe these processes in situ.

The loss of nanostructure due to reactive sintering in Al NPs based energetics such as nanothermite powders dramatically impacts the combustion of the composite and, as a result, burn times of the materials do not significantly shorten as a function of diameter and small particle sizes [53–55]. Other studies have shown that the fractional scaling law observed for the gas phase burning of nanoparticles can be corrected by considering sintering effects prior to burning [66]. Dynamic transmission electron microscopy (TEM) used to observe morphological changes in Al/CuO nanothermite aggregates found the creation of phase-separated adjoining spheroids occurs on the order of $\sim 0.5-5\,\mu s$, a range observed to depend on the aggregate size (Figure 9.2) [67]. However, the heating, in this case, was by a laser, and its thermometry was unavailable. Even though the reactive sintering phenomenon was speculated in a motionless heating stage TEM and was simulated by the related models, the direct observation of a dynamic reactive sintering process and subsequent propagation process in a nanothermite is still very challenging.

As we mentioned previously, thermites are a class of energetic materials whose reactivity can be systematically adjusted by changing chemistry (e.g. stoichiometry, reactant choice), particle size, mixing state, and architecture/morphology. Changes in chemical composition can be employed to manipulate the reaction mechanism as a means to modulate performance, while the latter variables are more related to physical effects such as heat transfer and interfacial surface area. However, these factors are inherently entangled since the heat transfer rates can impact reaction rate and vice versa, making it difficult to independently probe these effects. Numerous studies have been conducted with various approaches to directly observe the reaction dynamics of the nanothermites, but none have been able to practically probe a propagating reaction front or reactive sintering on a time or length scale commensurate with the phenomena. Some macroscale studies of thermite reaction dynamics
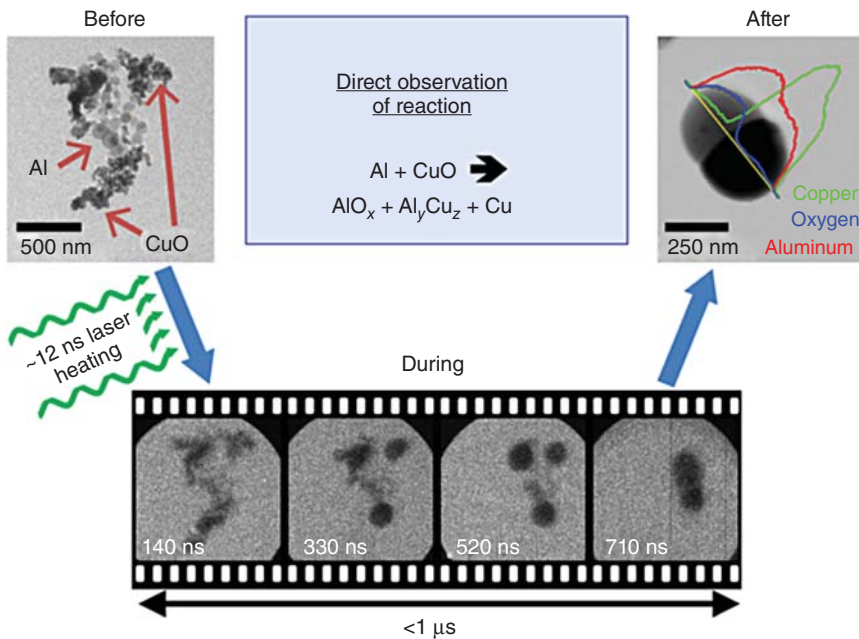
Figure 9.2 Nanothermite materials heated in situ at $\sim 10^{11}$ K s^{-1} showed significant morphological changes on timescales of 1−5 µs. The reaction between metallic fuel and oxygen carriers produced by the laser heating of aluminum and copper oxide (CuO) nanoparticles (NPs) was investigated (NPs) using movie mode dynamic transmission electron microscopy (MM-DTEM), which enables multi-frame imaging with nanometer spatial and nanosecond temporal resolution. Source: Egan et al. [67], Reproduced with permission from AIP Publishing.

have been captured by T-Jump/time-of-flight mass spectrometer (TOFMS) developed by Zhou et al. [68], which rapidly heats ($\sim 10^5$ K s^{-1}) material and can provide time resolve ignition and reaction products profiles (Figure 9.3). Another commonly employed device in our lab to quantify reaction dynamics in bulk materials has been a specially modified constant volume combustion cell [69] to simultaneously measure the pressure and optical emission histories of a nanothermite reaction. However, while these measurements provide useful insight on the energy release rate and reaction mechanisms in materials on the appropriate reaction time scales ($\sim$µs), they are unable to capture the dynamics and observe the reaction at the particle length scale (µm/nm).

High-speed imaging is quite useful in assessing various combustion regimes as it is the most direct method to interrogate the complexity of such heterogeneous systems during reaction [63–65, 70–72]. Due to the higher flame temperature and burn rate of nanothermites compared to solid propellants, it is difficult to probe the reaction in a high spatial and temporal resolution. To our knowledge, a fast-response and in-operando technique have yet to be employed to observe nanothermite reactions at resolutions high enough to resolve particle-sized phenomena and on the reaction time scale ($\sim$µs). In this section, we describe high-speed microscopy and
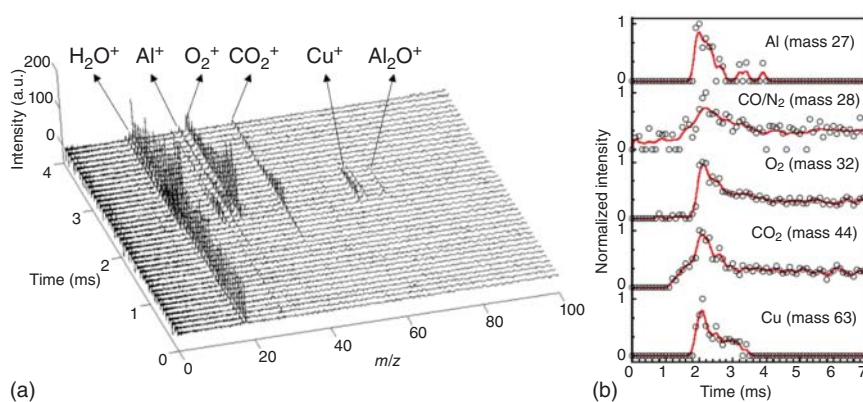
Figure 9.3 Time-resolved mass spectrum (a) and peak intensity (b) of gas species from rapid heating of Al/CuO. Heating rate ~5×10^5 K s^{-1}. Source: Reprinted with permission from Zhou et al. [68]. Wiley Publishing.

pyrometry, which we found to be a useful technique to observe the propagation of printed nanothermites [70–72] at high spatial (μm) and temporal (μs) resolution.

Figure 9.4a shows the major configuration of this study for microscopic characterization, in which a key point is employing a 40 times microscope objective coupling with a high-speed video camera. The microscope objective was focused on the backside of a cover glass slide on which the sample film was printed, thereby allowing the visualization of the flame front without the generated products obscuring the view. With the microscope objective, the pixel/size ratio was ~1 μm/pixel. At this resolution, the flame front (Figure 9.4b,c), as well as a single agglomerating particle (Figure 9.4d,e), could be captured and the corresponding temperature map (Figure 9.4c,) could be obtained. The area was labeled by a thin marker before the ignition, thus allowing us to find the exact area later in a scanning electron microscope (Figure 9.4e). A summary of the kind of information is shown in the panel of images below: Read from right to left are a snapshot taken from a single video frame (Figure 9.4b), the corresponding temperature map (Figure 9.4c) of the corresponding frame, temperature of single agglomeration particle showing a thermal gradient within a particle (Figure 9.4d), and finally the same particle imaged under scanning electron microscopy (SEM) with its energy dispersive spectrometry (EDS) map (Figure 9.4e).

In this chapter, we summarize our recent results about Al/CuO nanothermite composites to systematically show our understanding of how agglomeration affects the propagation rate. Firstly, we developed a universal ink formulation that enables 90 wt% nanoparticle loading with only 10 wt% polymers. Secondly, we extend our understanding of the agglomeration process and its relation to the propagation of Al/CuO nanothermite composites, through an in-operando high spatial (μm) and time (μs) resolution imaging system with pyrometry. Lastly, based on these findings, several approaches to engineer the agglomerations and propagations of Al NPs-based high particle loading nanocomposites are proposed.
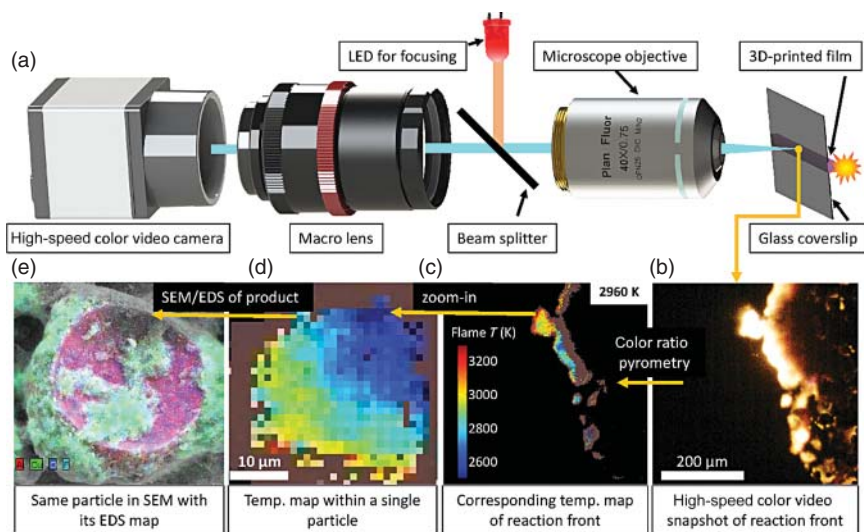
Figure 9.4 (a) Schematic showing high-speed microscope imaging of 3D-printed reactive materials. Read from right to left: (b) High-speed color video snapshot of reaction front; (c) Corresponding temperature map of reaction front; (d) Temperature map within a single particle, and (e) the same particle in SEM with its EDS map. Note: CAD models from Thorlabs (camera and microscope objective) and Ilirjan Leci (macro lens). Source: Wang et al. [73]. Springer Nature, CC BY 4.0.

9.2 Printing High Nanothermite Loading Composite Via a Direct Writing Approach

In this chapter, a simple direct writing approach is employed to print various high Al/CuO loading composite sticks for further characterizations. We develop an ink formulation for 3D printing with ≤10 wt% polymers mixture, which is used to load a total amount of ≥90 wt% nanoparticles. The ability of loading such high percentage of nanoparticles opens up new avenues for the practical applications of 3D printing on energetic materials including propellants, explosives, and pyrotechnics, which have far been unavailable. Adjustment of different energetic materials composition, fuel, and oxidizer equivalence ratio, the measured burn rate, flame temperature, as well as the energy release rate, can be easily tuned significantly. To load nanoparticles in a binder with direct-writing 3D printing, the binder needs to be soluble and its solvent should also have a reasonable boiling point and vapor pressure, to enable its easy removal during the printing, and to ensure safe processing. The ink should also be shear thinning to be extruded easily to make it printable, but beyond this, at such high loadings, unless an extended network is generated, the material will effectively print as a powder with no cohesive strength. Thus the resulting structure should have a mechanical integrity suitable for the application of interest.

We found that to satisfy both the reactive and structural requirements required two binders; a polymer hybrid of hydroxy propyl methyl cellulose (HPMC) and
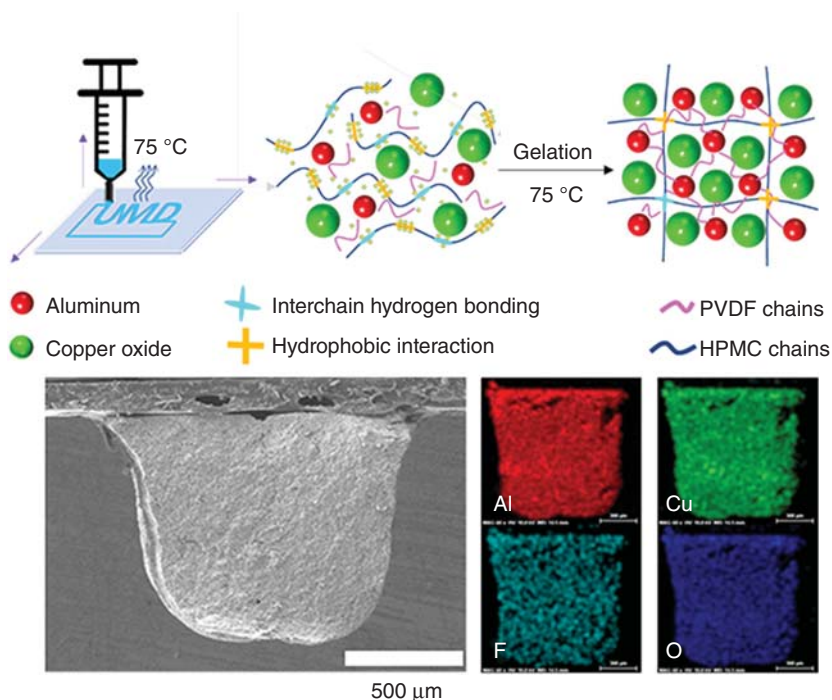
Figure 9.5 Gelation process in 3D printing (upper); Cross-sectional SEM and EDS results (lower) of printed Al/CuO high loading (90 wt%) composite sticks; PVDF: HPMC mass ratio is 2 : 3. Source: Wang et al. [71], Reproduced with permission from John Wiley & Sons.

polyvinylidene fluoride (PVDF) with a mass ratio of 3 : 2. Both polymers are soluble in dimethyl formamide (DMF), and the hybrid mix was found to be very stable with no evidence of separation. PVDF was employed as a polymeric binder since it doubles as an oxidizer and improves the ignitability of the composite *by* promoting the preignition of Al relative to other soluble fluorine-containing polymers such as Viton and THV [74]. HPMC was chosen since it is known to gel via hydrophobic interactions occurring between hydrophobic segments of the polymer chains upon thermal treatment. The very low mass loading of HPMC employed mitigates the fact that it has minimal energy content. This effectively is increasing the degree of crosslinking between polymer chains, forming a continuous 3-dimensional network [75], as schematically shown in Figure 9.5. The apparent viscosity of pure polymer solution is in the scale of 10 Pa s and dramatically increases by two to three orders of magnitude upon addition of solids. However, and most important for this application, the ink viscosity is highly dependent on shear rate. These inks show shear-thinning behavior at a shear rate > 0.05 1/s, with a sharp decline over several orders of magnitude. The ink was directly written on a preheated (~75 °C) glass plate. This thermal treatment is implemented to induce the gelation of HPMC, and evaporation of the solvent (DMF) to form a complete dry layer before a second layer is written [75].

The printing is in predesigned patterns that can be peeled off from the substrate and cut into ~3 cm long sticks for burn rate measurement. The mechanical properties of the sticks are close to that of pure polytetrafluoroethylene (PTFE) [76], confirming the 90% loading nanothermite composite is mechanically strong. For the *fuel-lean* and stoichiometric Al/CuO case, the density was found to be ~2.1 and ~1.8 g cm^{-3}, respectively, which is ~1/3 of the theoretical density. With the increase of Al content, the theoretical and actual density declined gradually owing to the lower density of Al compared to CuO, however, the porosity remains constant at ~66%. While this may seem low, in fact, the theoretical maximum packing density of nanoparticle aggregates is effectively this number, implying that the composite cannot be made denser [77, 78]. A higher packing density could be achieved if the nanoparticles are preprocessed to break the aggregates. The SEM and EDS images (Figure 9.5) of the cross-sectional sticks also confirm the close packing and intimate mixing of Al/CuO in the printed sticks.

For the pure thermite Al/CuO, the adiabatic flame temperature is estimated as ~2840 K and is limited by the boiling point of Cu (~2835 K), one of the major reaction products [79]. The flame propagation snapshots of the burning composite sticks (~3 cm) with normal (Figure 9.6a) and low (Figure 9.6b) exposure (light exposure in high-speed camera) along with the flame temperature maps (Figure 9.6c), and the detailed time-resolved mean/median flame temperature profile (Figure 9.6d) are shown in Figure 9.6. The latter was obtained using a high-speed color camera pyrometry technique detailed in our previous study [74]. All combustion tests were conducted in 1 atm Ar to exclude the effect of additional oxygen [80]. The horizontally propagating flame (Figure 9.6a) indicates very vigorous combustion, generating many hot gas/particles and a bright flame. The flame fronts proceed steadily (Figure 9.6a–c) with time and demonstrate a stable linear burn rate of ~3 cm s^{-1}. The flame temperature remains steady over the length of the burn at 2500–3000 K, and most points are located approximately at ~2800 K. This result is interesting in that it implies we can print a thermite-based material that has a measured flame temperature close to that theoretically expected (~2843 K) and implying the polymer is not impeding the combustion completeness [79]. However, from these snapshots at a resolution near ~100 μm per pixel, it is difficult to observe the Al agglomeration process, and more advanced diagnostic techniques are required for details.

Generally, for a nanothermite, peak reactivity is achieved at or near stoichiometric [81]. Figure 9.7 presents burn rate and temperature measurements as a function of the Al/CuO ratio at 90% loading. The flame temperature peaks at ~22 wt% of Al corresponding to the stoichiometric case ($\Phi = 1$), while the linear burn rate peaks fuel-rich (Figure 9.7), which is probably due to the enhanced gas production and heat convection with more reactive fuel [66, 79, 82]. The relative energy release rate (normalized heat flux Q') in Figure 9.7 peaks between the maximum flame temperature and burn rate implying that if optimization of energy release is desired, a fuel-rich formulation ($\Phi = 1.5$–3.5, 30%–50% Al content) is necessary. The calculation of relative energy release rate is as follows:

$$Q' = \frac{Q}{t} = \frac{m \times C_p \times \Delta T}{t} = \frac{\rho \times L \times A \times C_p \times \Delta T}{t} = (A \times C_p) \times \rho \times \left(\frac{L}{t}\right) \times \Delta T$$
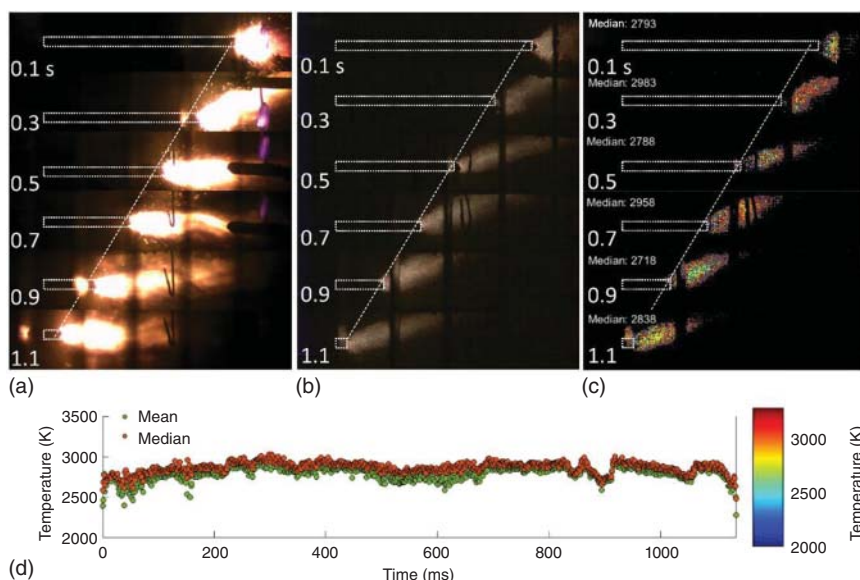
$$(9.1)$$

Figure 9.6 Burning snapshots with normal exposure (a), low exposure (b), and the measured temperature map (c) and curve (d) with time for 15-layered stick with 90 wt% Al/CuO nanothermite loading (6 wt% Methocel, 4 wt% PVDF, Al in Al/CuO is 22 wt%). White dotted rectangles represent the burn stick. Source: Wang et al. [71], Reproduced with permission from John Wiley & Sons.
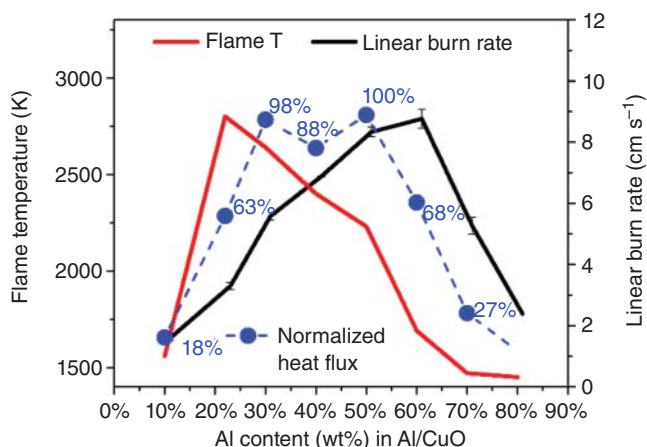

Figure 9.7 Linear burn rate, flame temperature, and normalized heat flux of the burning sticks with 90 wt% nanothermite loading (with different Al content in Al/CuO from 10 to 90 wt%). Source: Reprinted with permission from Wang et al. [71], Wiley Publishing.

where Q is the energy release, C_p is the heat capacity, and T is the flame temperature. ρ is the density, t is the time, A is the cross-sectional area, and L/t is the velocity (ν). If we are assuming the cross-sectional area and heat capacity of different composites are roughly the same, the relative energy release rate (Q') is proportional to $\rho \times \nu \times T$.

In summary for this section, we developed an energetic ink formulation with a particle loading of 90 wt%, which can be used for direct writing of 3D structures. The key additive in the ink is a hybrid polymer of PVDF and HPMC, in which the former serves as an energetic initiator, and the latter is a thickening agent and a binder that can adhere to the particles with a small percentage of polymer. The best polymer ratio (best printing resolution) was found to be 4 wt% PVDF and 6 wt% HPMC enabled particle loadings as high as 90 wt%. The rheology shear thinning properties of the ink was critical to making the formulation at such high loadings printable. The Young's Modulus of the printed stick is found to compare favorably with PTFE, with a particle packing density at the theoretical maximum. The linear burn rate, mass burn rate, flame temperature, and heat flux were found to be easily adjusted by varying the fuel/oxidizer ratio. The average flame temperatures are as high as ~2800 K with near-complete combustion being evident upon examination of the post-combustion products. As we change the equivalence ratio of Al/CuO, the burn rate, flame temperature, and energy release rate vary significantly, as well as the flame structure and Al agglomeration status. It is important to look into these factors in more advanced diagnostic techniques to find out the fundamental mechanism behind this. The Al/CuO high-loading composite sticks ($\Phi = 1$) present in this section are used as the reference (baseline) for the following studies.

9.3 Agglomerating in High Al/CuO Nanothermite Loading Composite

9.3.1 In-Operando Observation of Flame Front

Figure 9.4b show a typical flame front snapshot of the Al/CuO nanothermites (90 wt%) captured in a window of $512\,\mu m \times 512\,\mu m$ with a frame rate of ~18 000 (55.5 μs per frame) and the corresponding flame temperature map (Figure 9.4c) was obtained by a color camera pyrometry through image processing. We can see the flame fronts consist of stochastic bright spots, which discontinuously propagate the reaction. These bright areas are roughly divided into a leading flame front and the following cooling zone, as distinguished by the brightness. The noticeably brighter area spanning ~30 μm was confirmed to be the leading edge from the measured temperature ~ 3000 K, which is close to the previously measured reaction temperature of Al/CuO [80].

Reactive sintering, as discussed above and previously observed [56, 57, 66, 67], is the coalescence of aggregated and/or agglomerated nanoparticles driven by heat released during the reaction and results in the effective loss of nanostructure. As Figure 9.4d shows, after the flame front has passed any given area, the sintered particle with a mean diameter of ~20 μm is observed. It is also notable that the flame front thickness is roughly the same size as the agglomeration size, a reasonable observation considering that these flame fronts were constructed by networks of individually sintering particles propagating the reaction by either advection or heat release.

9.3.2 Mapping Optical to Electron Microscopy of Agglomeration

To investigate the morphology, composition, and size distribution of the post-combustion product, the reaction product-coated slide was examined by SEM and energy EDS. As shown in Figure 9.4e, we were able to find an exact one-for-one correspondence between the *in-operando* microscope imaging and the SEM image. It is also notable that we can achieve a dynamic *in-operando* temperature measurement of a single sintering particle on the resolution of μm. Furthermore, there is a ~1000 K temperature difference across the particle at a distance of ~30 μm, which indicates a temperature gradient of $3 \pm 1 \times 10^7$ K m^{-1} and in the same direction as the flame propagation in this area. From the EDS results, we also concluded that the main composition of the sintered particle is Al_2O_3 (~20 μm) and the coated smaller particles are Cu (<20 nm). Such small Cu nanoparticles indicate that Cu was vaporized during the reaction due to a flame temperature ($\geq$2900 K) above the boiling point of copper (2835 K).

To further explore this difference between micro and macro scales, a group of sintering particles was closely monitored as a bridge between reactive sintering and flame propagation. In Figure 9.8a, flame propagation is from right to left. An initial burning spot (frame 2) spreads to the surrounding area, where another two sintered particles appear. However, before cooling, the adjacent area on the left-top and right-bottom are observed to ignite and then move to the left. The schematic of the above process is demonstrated in Figure 9.8b and the final sintered particles are shown in Figure 9.8c. Even though reactive sintering occurs in ~μs, the propagation of the reaction is relatively slow and limited by the heat conduction and high ignition temperature of Al/CuO (~1000 K) [57] which in the microscope temporal image shows an almost stochastic behavior, despite the overall reaction front moving in a given direction. This suggests that density gradients set up local
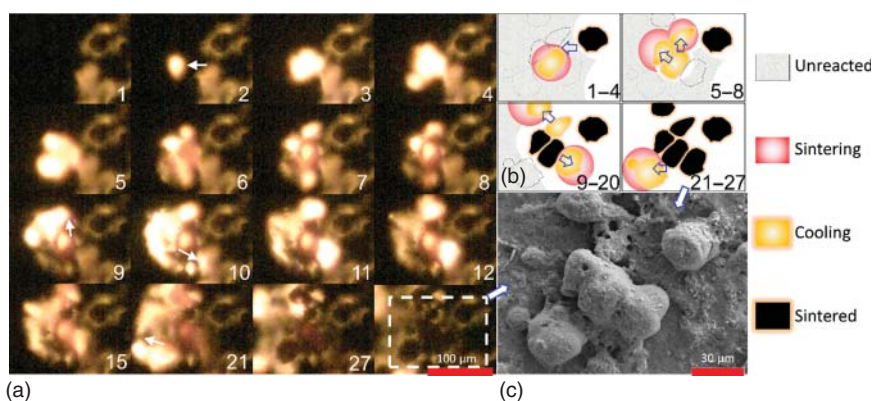

Figure 9.8 (a) Series of reactive sintering and ignition snapshots of a group of particles (labeled is frame sequence, 55.55 μs per frame) and (b) its corresponding schematic cartoon. Note: the marked arrows are propagating direction. (c) The corresponding SEM image of the sintered Al_2O_3 particles coated with Cu nanoparticles, as evident by the EDS results. Source: Wang et al. [73], Springer Nature CC BY 4.0.

sintering regions which comprise heat generation centers. These centers transport energy to neighboring areas that ignite. In this way, propagation is very similar to the general concept of laminar flame theory in which flame velocity $\sim$ (thermal diffusivity $\times$ reaction rate)$^{1/2}$. The difference is that the macro scale reaction velocity is limited by the thermal diffusivity between the sintered heat sources.

9.3.3 Agglomeration Affects the Propagation Rate

To evaluate the above argument, consider that during the passing of the reaction front (i) reactive sintering, (ii) cooling, and (iii) a final sintered product is observed. The fact that the flame front consists of these different stages implies an inhomogeneous reaction front with different heat fluxes (Figure 9.9a,). We can estimate heat flux $\sim$ thermal conductivity $\times$ temperature gradient $= 10^9$ W m^{-2} in the reactive sintering stage based on the measured temperature gradient and an estimate thermal conductivity for Al/CuO ~ 60 W m^{-1} K^{-1}. This large high heat flux supports a rapid front propagating with a velocity as high as ~ 50 cm s^{-1}. However, when reactive sintering has mostly completed (cooling stage), the heat flux declines by ~ 3 orders of magnitude to 10^6 W m^{-2}, owing to the much lower thermal conductivity of gas (0.1 W m^{-1} K^{-1}) which separates the reacted from unreacted material. Thus, while we see local rapid reaction these reaction events are slowed down by low conductivity zones resulting in an over propagation rate that is considerably lower (Figure 9.9b). This calculation indicates that the heat flux in the cooling stage in a reactive sintering process is critical to the macroscale flame velocity.

In this section, high-speed microscopy/thermometry enables us to observe them in-operando micro reaction of Al/CuO nanocomposite thermites. We could visualize the agglomerating process (reactive sintering) in nanothermite reaction in high spatial (~ 1 µm) and temporal (~ 55 µs per frame) resolutions. The temperature map of the flame fronts and the agglomerating particles were also obtained by a color camera pyrometry of the same images. The flame front thickness was determined
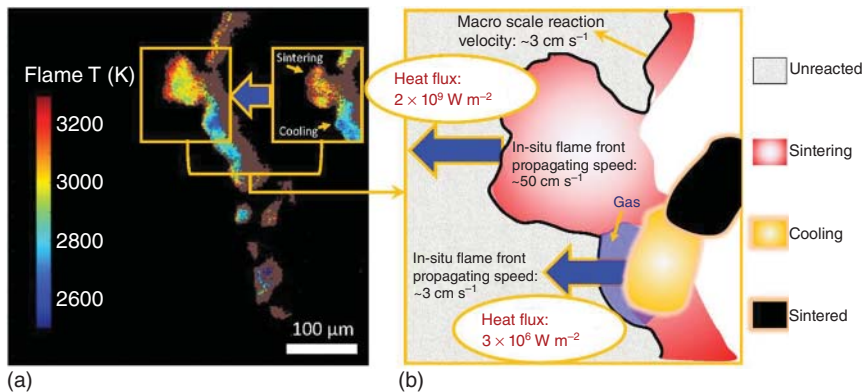

Figure 9.9 (a) Two typical temperature map snapshots of flame front of Al/CuO nanothermite and (b) the schematic showing of heat flux distribution from different stages of reactive sintering particles. Source: Wang et al. [73]. Springer Nature, CC BY 4.0.

from the above results as ∼30 μm, which is the same size as the Al agglomeration. Post-reaction analysis of the same area and the corresponding sintered particles were found in the scanning SEM, which enables one-to-one composition mapping. For these studies, we can conclude that the local reaction velocity is an order of magnitude higher than macroscale flame velocity. These results imply that local heat generation with sintering particles limits heat transport to neighboring areas. Heat flux calculations indicate that the macroscale flame velocity was highly dependent on the heat release rate in the cooling stage in a reactive sintering process.

9.4 Engineering Agglomerating and Propagating through Oxidizer Size and Morphology

9.4.1 The Concept of a Pocket Size

The connection between propellant microstructure, agglomerations, and burn rate was first identified in the 1960s by Povinelli and Rosenstein, who compared the effect of oxidizer size on collected agglomerations and burn rate [83]. The heterogeneous nature of agglomerating was also addressed by a "pocket" model. A "pocket" region (Figure 9.10) is where an agglomeration finds a privileged location to take place [84–86]. Cohen [85] established some rules for the definition of final agglomerate size based on local flame temperature and encapsulation criteria, disregarding the random nature of the propellant microstructure. In this section, we are going to change the "pocket" size of Al aggregates by packing them with different sizes and morphology CuO to engineer the Al agglomerations size.

In this section, three different CuO oxidizers were explored in this study with both 100% and 90% thermite loadings: ∼5 μm diameter microparticles (CuO MPs),
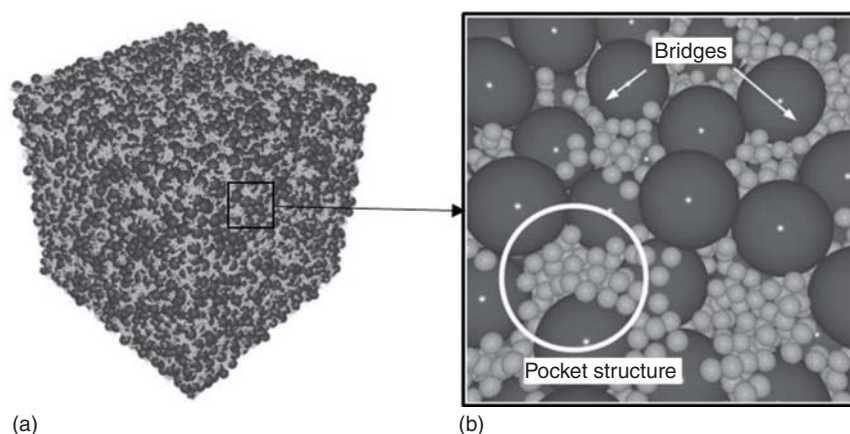

(a) (b)

Figure 9.10 Microstructure of a propellant model replicating an Oxidizer/Metal/Binder propellant (61/12/27 vol%, 68/18/14 mass percent). Oxidizer size: 150 μm (dark spheres). Metal size: 30 μm (bright spheres). Source: Reprinted with permission from Ref. [84]. Copyright 2015, by F. Maggi.
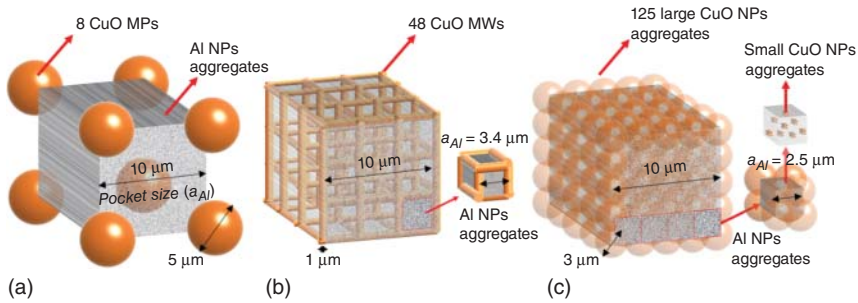
Figure 9.11 Schematic illustrating the "pockets" of Al in Al/CuO composites with different CuO morphologies – MPs (diameter 5 μm), MWs (diameter 1 μm, length 15 μm) and NPs (diameter 3 μm). The resulting pocket size of different composites is labeled as ∼10, ∼3.4, and ∼2.5 μm. Source: Reprinted with permission from Wang et al. [87]. Elsevier Publishing.

∼15 μm (length) × 1 μm (diameter) microwires (CuO MWs), ∼40 nm diameter nanoparticles (CuO NPs) [87]. In particular, the CuO MWs have a calculated equivalent spherical volume diameter of ∼3 μm, so the CuO MWs and CuO MPs are roughly the same volumes. Nevertheless, the calculated specific surface area (per mass) varies widely and can be ranked as CuO NPs (125) ≫ CuO MWs (7) > CuO MPs (normalized to 1).

Herein, we construct a simple model of the pocket size of the three different Al/CuO composites with CuO MPs, MWs, and NPs. The "pocket" of Al NPs is assumed to be a cube whose size is determined by the density and size of the different CuO morphologies employed, which constrains the "pocket." The "pocket-size," (a_{Al}), is the length of the cube (pocket). As shown in Figure 9.11a, to estimate the size of the pocket in the three cases, the volume (Vol.) ratio of Al to CuO was used. To account for the known lower packing density of fractal aggregates [78], the volume of Al and CuO NPs aggregates was increased 3×. For Al/CuO with CuO microparticles and microwires, the Al/CuO volume ratio is 1.95 and 0.65 for Al/CuO with CuO nanoparticles.

The volume-based equivalent diameter (Φ_{CuO}) of CuO MPs and MWs is ∼5 and 2.8 μm, respectively. The original size of CuO NPs is ∼40 nm and the aggregate size of CuO NPs was estimated as ∼3 μm based on SEM observations. Assuming a cubic control volume of 10 μm sides, we will have 8 CuO MPs (8 corners in the cube), 48 CuO MWs (4 × 4 × 3), and 125 CuO NPs (5 × 5 × 5) for this superlattice to construct the structure in Figure 9.11. The size of the smallest confined pocket unit (a_{Al}) of Al NPs in CuO MPs, CuO MWs, and CuO NPs are ∼10, ∼3.4, and ∼ 2.5 μm, respectively (Figure 9.11).

9.4.2 Reducing Agglomeration with CuO Wires

We begin with the microscopic burning images of the CuO MPs-based thermite (90 wt% Al/CuO sticks). The reaction front shows the formation of large, highly emissive, molten droplets (2100–2800 K) formed on the surface (dash lines) of the composite sticks (Figure 9.12a). The temperature of these spheres is significantly

higher than the melting point of Al (melting point, MP: 933 K) and CuO (MP: 1600 K) and the formation of spheres confirms they are made up of molten matter. These droplet spheres continually grow in size from the coalescence of smaller droplets driven by surface tension before lifting off from the burning surface (Figure 9.12a–c). The lifting off only occurs just after the Al_2O_3 cap is observed in the droplets and the temperature approaches ~2400 K (Al_2O_3 melting point) [58–63]. The process of coalescence is rapid (<~0.1 ms) and consistent with the timescale we have observed above [73].

The same basic processes appear to be taking place for the CuO MWs and NPs cases (See Figure 9.12b, respectively). However, differences in agglomeration size are obvious in the images and are quantified in the size distribution histograms shown in Figure 9.12a-1~c-1. In both the CuO MW and NP cases, the droplet sizes are much smaller compared to the CuO MPs case (~15 versus ~40 μm). Consistent with the coalescing size in Figure 9.12, the post-combustion residues also confirm that the residue size of CuO MPs case is ~5–10 times larger than that of CuO MWs and NPs.

In summary, we see that the MWs have a behavior closer to that of the NPs over that of the MPs in both microscopic and macroscopic scales. We must now ask why microwires produce such small droplets in comparison to microparticles. There are many complex phenomena involved, but one possible explanation is inspired by the "pocket model" theory where the volume of the agglomerated particles produced is predominately controlled by the effective volume of Al particles that can be aggregated within a surrounding oxidizer matrix (depicted in Figure 9.11) [84–86, 88].

As schematically shown in Figure 9.11, the CuO MWs with a high aspect ratio have ~1/30 smaller pocket volume (a_{Al}^3) compared to the CuO MPs. The point is that the smaller pocket limits the effective size of the Al aggregate that can be formed during combustion [78]. If we assume that the pocket operates independently due to the gas generation of CuO (which can break apart sintered aggregates), we can estimate the size of the resulting sintered Al particle since we know that the packing density of Al fractal aggregates in the pocket is ~35% [71, 78]. Based on this, the diameter of the average Al sintering size (Φ_{Al}) from the corresponding "pocket" can be calculated as 8.8, 2.9, and 2.2 μm for MPs, MWs, and NPs, respectively ($\Phi_{Al} = 0.874a_{Al}$).

This result indicates that the microwires should yield Al sintered particles that are about the same size as those generated from composites made with CuO NPs, and about a factor of three smaller than those formed during reactions with CuO MPs. This is qualitatively consistent with the experimental observation (see histograms in Figure 9.12). Our calculated particle sizes are smaller than measured, however, this is expected since the assumption of independent pockets is a gross approximation. Nevertheless, the trends are unambiguous.

9.4.3 Promote Propagating through Using CuO Wires

Figure 9.12 also shows that the molten droplets in the cases of the CuO MWs and NPs (~1.2 m s^{-1}) are ejected with higher velocity than the CuO MP case (~0.4 m s^{-1}). The differences in molten droplets velocities suggest higher gas generation rates, and thus faster reaction, and are consistent with the macroscopic flame propagation
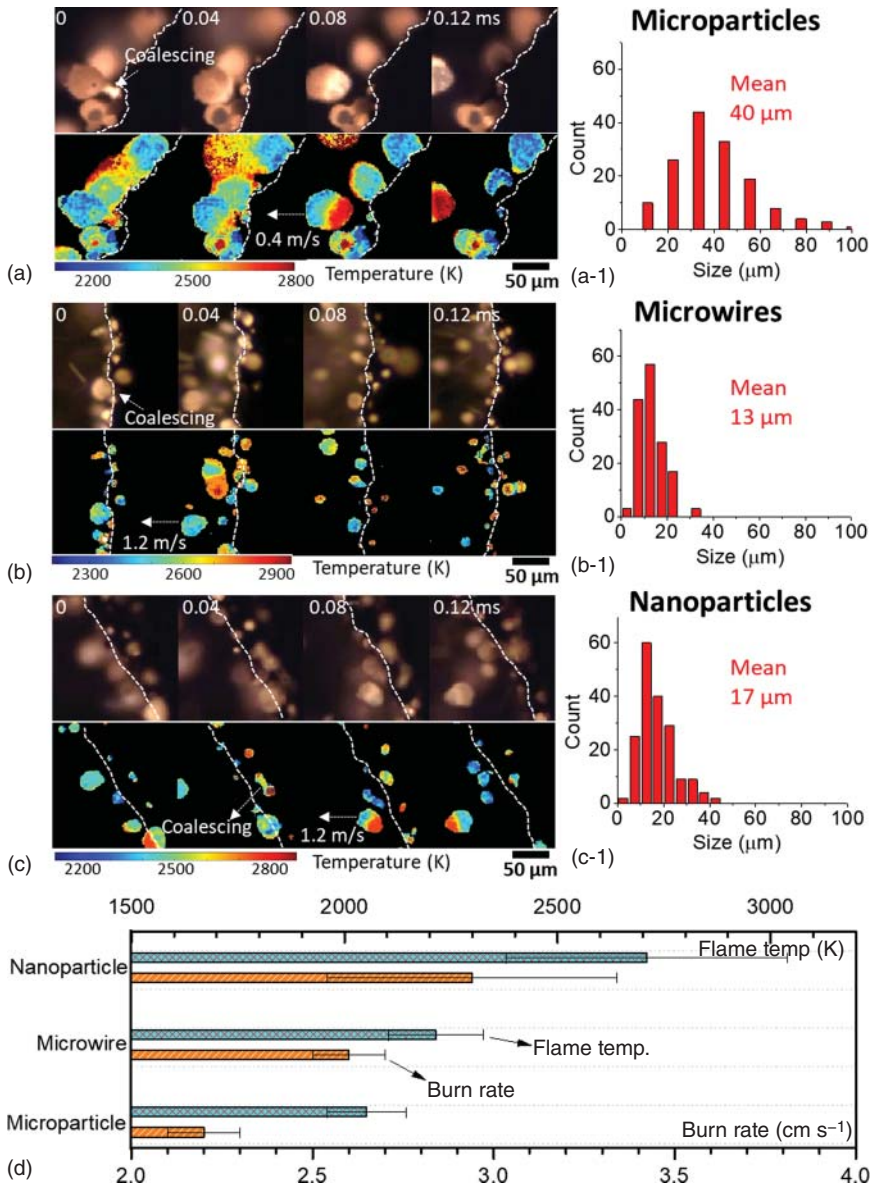
Figure 9.12 The evolution of agglomerations (a–c) with different size distributions (a-1~c-1) was observed in the microscopic burning surface of Al/CuO composite sticks (90 wt%) with CuO microparticles (a), microwires (b), and nanoparticles (c). The sizes of the agglomerations were measured and averaged based on >150 agglomeration droplets in the high-speed videos. Summary of burning rate and flame temperature (d). Δt is ~42 μs between two neighbor frames. Source: Wang et al. [87], Reproduced with permission from ELSEVIER.

results. As shown in Figure 9.12d, the burn rate and flame temperature ranked as CuO NPs > CuO MWs > CuO MPs. The higher temperature for the nanomaterial is not surprising as it suggests more complete combustion.

To more directly demonstrate the effects of CuO size and morphology on thermite propagation, we 3D-printed Al/CuO ink on a glass slide to form a thin thermite film without using any binder. The thermite film is very brittle but could hold its integrity during testing. We estimated their relative density to be 1 (CuO MPs), ∼0.83 (CuO MWs), and ∼1.07 (CuO NPs), based on their thicknesses (weight and width/length is the same). With CuO MWs and NPs, the films burn at an average speed of ∼55 and ∼33 m s^{-1}, respectively, which is >15× higher than Al/CuO with CuO MPs (∼2 m s^{-1}). Moreover, the flame temperatures of CuO MW- and NP-based thermites are measured as ∼3000–3200 K, respectively, which is ∼500 K higher than that of the CuO MPs case (∼2550 K).

9.4.4 Polymer Addition Significantly Reduces the Micro-Explosion of the Agglomerations

A notable observation in this study is that only 10 wt% polymer reduced the burn rate of Al/CuO with microspheres by the 2 orders of magnitude (∼2 m s^{-1} versus ∼2 cm s^{-1}). It is likely that this decrease in propagation rate could be attributed to the polymer acting as a heat sink. A recent study by our group suggests that the agglomeration is only able to transfer a small fraction of the energy required to ignite nearby unreacted regions when considering the polymer and reactants in the burn sticks [72]. However, if the polymer was removed from consideration (as it is in the powder cases), the amount of energy required to ignite unreacted areas decreases, therefore the role of agglomeration as an energy transfer and propagation method becomes more significant. Whereas the agglomeration in the burn stick case provides a limited enhancement in propagation via advection, it is more effective as a heat transfer mechanism and can increase the propagation rate in the thermite powder case.

The polymer used in this section acting as a heat sink also seemingly plays a role in the number of micro-explosions happening in these agglomerations, which further enhance the reactivity. When examining the microscopic combustion videos of the Al/CuO microsphere composite films (100 wt%, no polymer), clear evidence of bubbling and micro-explosions. A complete picture of the overall process which illustrates the coalescing, bubbling, and micro-explosion process, and a schematic cartoon is shown in Figure 9.13. Agglomerations are seen to coalesce and grow into larger droplets within ∼0.1 ms, and subsequent bubbling and micro-explosions to start a new cycle of this process. Micro-explosions are known to play a significant role in enhancing reactivity by creating smaller structures with higher surface areas. It is noted that no clear micro-explosion was observed in the low reactivity Al/CuO microsphere burn stick sample (90 wt% reactive material), while the Al/CuO microsphere powder sample (100 wt% reactive material) has numerous clearly-defined micro-explosions in the burning videos (see supporting information).
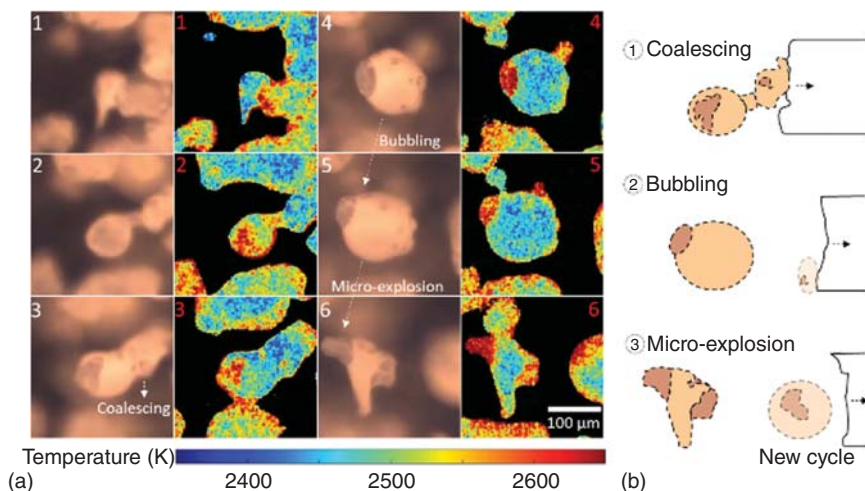
Figure 9.13 Coalescing, bubbling, and micro-explosion processes were observed in the 3D-printed Al/CuO (with CuO microspheres) composites (100 wt%, no polymer) on a thin glass slide. Δt is ~42 μs between two neighbor frames. Source: Haiyang Wang, Michael R. Zachariah.

The absence of micro-explosions in the Al/CuO microsphere sticks (10 wt% polymers) burning could be attributed to a ~500 K decrease in flame temperature (mean: ~2050 K) compared to the pure thermite composition (mean: ~2550 K), which makes the vaporization of CuO (boiling point: ~2270 K) much less likely to happen. As the thermite reaction proceeds, the temperature of the molten particles exceeds the boiling point of Al (2743 K) and Cu (2835 K), which causes more micro-explosions to enhance the reactivity.

In summary, the polymer addition to the thermite powder negatively impacts the propagation rate in two ways: (i) the polymer acts as a heat sink which reduces the flame temperature and, in turn, reduces the number of micro-explosions, and (ii) the thermal mass of the polymer makes the energy transferred via advection of micro-explosion byproducts less impactful.

9.4.5 Summary

In this section, high-speed microscopy and pyrometry on a ~μm space and ~μs timescale were used to observe agglomeration from Al/CuO thermite combustion with different oxidizer particle sizes and shapes (microparticles, microwires, and nanoparticles). We found that CuO microwires rather than microparticles make the propagation velocity and the extent of agglomeration behave more like CuO NPs. The agglomeration size in the microscopic burning of the 3D-printed Al/CuO composites was found to be reduced from ~40 to ~13 μm when replacing microparticles with microwires. A simple mechanism based on the "pocket model" was employed to explain why CuO microwires-based thermite produces smaller agglomeration and higher energy release rate. In Al/CuO nanothermite without polymers, replacing

CuO microparticles (5 μm) with similarly sized CuO microwires (equivalent diameter: 3 μm) was shown to dramatically elevate the burn rate by ∼27× (2 m s^{-1} versus 55 m s^{-1}) and increase the flame temperature from 2550 to 3200 K, resulting in ∼30 times higher heat flux (energy release rate). Adding 10 wt% polymers into the above three thermite systems slows down the burn rates from ∼m/s to ∼cm/s, and we proposed the polymer addition might act as a heat sink thus preventing/reducing the micro-explosions in the agglomerations in the loading nanothermite composites.

9.5 Engineering Agglomeration and Propagating through Restraining the Movement of Agglomerations

9.5.1 Adding Carbon Fibers to Promote Energy Release Rate in Energetic Composites

One approach for balancing mechanical integrity, potential energy density, and energy release rate, could be to incorporate additives. For example, replacing conventional binders with energetic ones [28, 74, 89–93] or applying catalyst embedded with ammonium perchlorate [94, 95]. Embedding reactive or metal wires is known to promote combustion [87, 96, 97]. New techniques and formulations have been introduced to increase energetic material content [14, 98] and control combustion behavior via alterations to chemical content [71, 99]. However, since these materials largely rely on nanothermites as their primary energetic component to maximize energy release, it is possible that energy is being inefficiently coupled back into the system to promote propagation given their longer reaction time [100]. Seeing as energy release rates in propellants are determined by how fast reactions occur, and how fast energy can be transferred to unreacted material, one could feasibly use thermally conductive materials as a method to improve heat transfer and energy release rate [101]. Additionally, mechanical integrity may be bolstered by incorporating fibers that have been widely employed to reinforce polymer-based 3D structures [102–105]. Should the thermally conductive additives be fibrous, they could serve the dual purpose of both increasing mechanical integrity and energy release rate [106–108]. In this study, we choose carbon fibers as the additives considering their high melting point (∼3700 °C) to hold their shape during the combustion and don't likely have catalytic effects on the other components (polymer decomposition, or Al/CuO reaction), to minimize the effect of possible chemistry between the fibers and the reacting species so that we could better probe the role of carbon fibers on the thermal/physical effects on flame propagation.

In this section, carbon fibers were embedded into ∼90 wt% loading Al/CuO nanothermite through a simple direct writing approach. With the addition of only ∼2.5 wt% carbon fibers, the propagation rate (burn rate) and heat flux of the sticks were promoted by more than a factor of two. From in-operando microscopic observations, the carbon fibers on the burning surface intercept ejected hot agglomerations, which can provide enhanced heat feedback to the unburnt materials on the flame front. This study provides insight for a new method to potentially accelerate the propagation of 3D-printed energetic composites.

9.5.2 Embedding Carbon Fibers into High Loading Al/CuO Nanothermite Composite

Carbon fibers with a diameter of ~7 μm, and a maximum length of ~3 mm were embedded into high loading (~90 wt%) Al/CuO nanothermite-printed sticks through a direct writing technique. As shown in Figure 9.14a, the carbon fibers are randomly dispersed in the ink and extruded through a blunt stainless-steel needle with an inner diameter of ~1.2 mm (16 gauge). As illustrated in Figure 9.14b, since the carbon fibers are longer than the inner diameter of the needle (>1.2 mm), they are aligned when passing through the needle during the printing process (Figure 9.14b) [71, 100–102, 105]. The morphology of the Al/CuO prints with embedded carbon fibers is depicted in an illustration and an optical microscopy photo in Figure 9.14c. A cross-sectional SEM image (Figure 9.14d) shows that the carbon fibers are generally embedded parallel to the direction of writing. More evidence of the predominantly parallel alignment of the carbon fibers in the Al/CuO
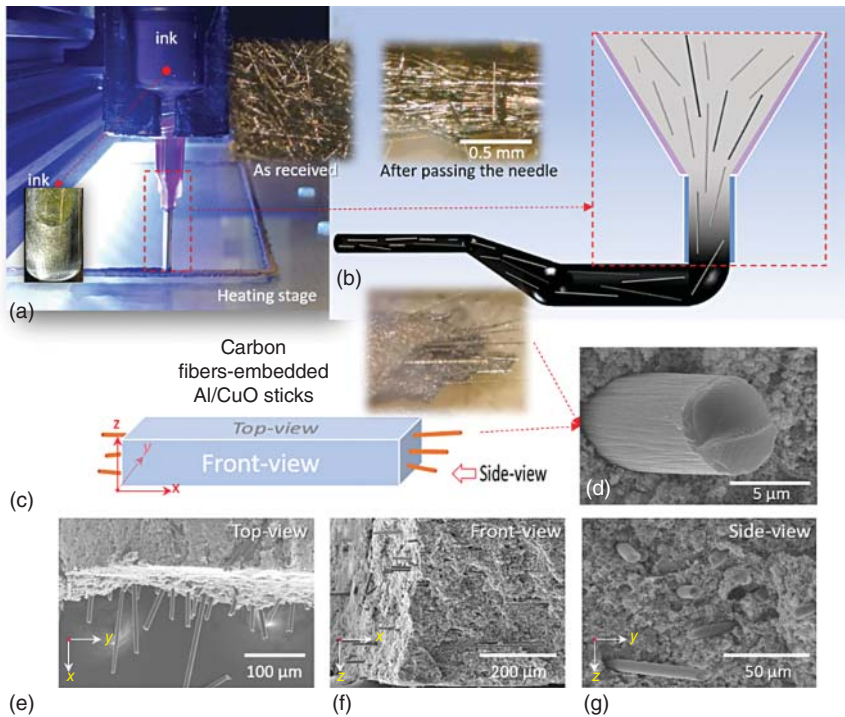

Figure 9.14 Optical image (a) and schematic showing (b) direct writing process of Al/CuO composite sticks containing carbon fibers; Optical images of randomly dispersed (right insert in a) and aligned carbon fibers (insert in b); Prepared ink for direct writing with carbon fiber (left insert in a); Schematic (c) and optical image (insert in c) of Al/CuO (90 wt%) composite sticks with aligned carbon fibers; SEM images of Al/CuO composite with carbon fibers on side view (d and g), top view (e), and front view (f). Note: the carbon fiber content is 2.5 wt%. Source: Wang et al. [109], Reproduced with permission from American Chemical Society.

composites is revealed when the printed sticks are viewed from different angles in the SEM (Figure 9.14e–g).

9.5.3 Enhanced Propagation of Al/CuO Composite with Carbon Fibers

Al/CuO composites with varied carbon fiber content (0, 1, 2.5, 5, and 10 wt%) were printed (cut into 3 cm long sticks, with a height of ~1 mm, a width of ~2 mm) and investigated by measuring propagation rates and flame temperatures in an inert atmosphere (1 atm argon). The macroscopic propagation events were recorded by a high-speed color camera with light exposure settings optimized to obtain the most color information while avoiding overexposure. Figure 9.15a,b show the typical time-resolved snapshots, from which we could obtain the flame propagation rates. The flame temperature of the combustion events was measured using three-color pyrometry [72, 80], and the corresponding temperature maps are shown in Figure 9.15a,b. From these images, one can see a ~350 K variation in flame temperature for materials with different amounts of carbon fiber addition. However, the change is relatively minor considering the errors in the measurement.

The propagation rates (average burn rate v = total stick length/total burn time) and the average flame temperatures (T = an average of all active points in a whole burning event) of the Al/CuO composites with different contents of carbon fibers are summarized and shown in Figure 9.15c. With the increase of carbon fiber content
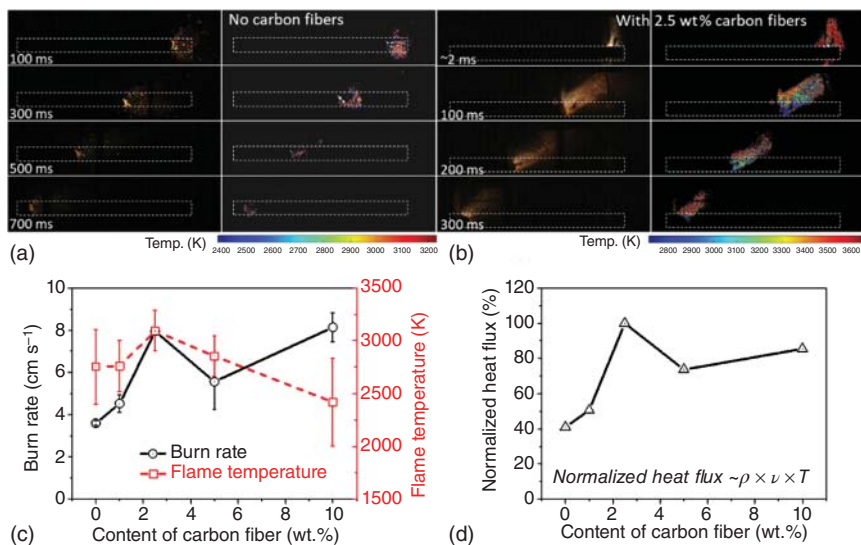
Figure 9.15 Macroscopic imaging snapshots of Al/CuO (Al/CuO is ~82–90 wt%, varying with different carbon fibers) composites without (a) and with 2.5 wt% (b) aligned carbon fibers; Summary of the burn rates and mean flame temperatures (c), the normalized heat flux (d) of Al/CuO composite prints with different contents of carbon fibers; The equivalence ratio of Al/CuO in this figure is 0.8. Note: the marked squares are where the Al/CuO-printed sticks were located. Source: Wang et al. [109], Reprinted with permission from American Chemical Society.

from 0 to 2.5 wt%, the burn rate rapidly increases from ~3.5 to ~8 cm s^{-1} and fluctuates from ~6–8 cm s^{-1} when the carbon fiber content is ≥5 wt%. This result supports the hypothesis of an increase in burn rate with the carbon fiber addition. With the increase of carbon fiber content, flame temperatures peak at ~2.5 wt% and decrease gradually from ~3100 to ~2400 K with the increase in carbon fiber content. Combined with measured densities (ρ) of the prints, we can estimate a normalized heat flux ($\sim\rho \times v \times T$, detailed in supporting information) and summarize the results in Figure 9.15d, which shows that ~2.5 wt% carbon fiber addition enhances the heat flux of the Al/CuO composites by ~250%. Although the snapshots in Figure 9.15a,b indicates that the flames are larger in the composites without carbon fiber additives, the apparent change in heat release suggests that there may be other interactions or modes of heat transfer on smaller length scales that are difficult to resolve with the macroscopic imaging apparatus (~70 µm per pixel).

9.5.4 Enhanced Heat Feedback and Heat Transfer with Carbon Fibers: Restraining the Movement of Agglomerations

To probe reaction dynamics at the flame front, a high-resolution microscopic imaging system (~1.7 µm per pixel) coupled with pyrometry software was employed to closely observe the reaction in a small area of ~1 mm^2. As seen in Figure 9.16a, the reference Al/CuO composites without any carbon fiber addition show growing agglomerations on the burning surface that are up to ~100 µm. As Figure 9.16a shows and Figure 9.16b illustrates, since most of the hot agglomerations are flying away from the burning surface, the heat feedback from these particles to the unreacted material will be relatively low and slow in comparison to those particles that are physically in contact and within the local proximity with the reacting surface. By contrast, the embedded carbon fibers (2.5 wt%, Figure 9.16c), appear to "catch" particles that were being ejected. With the hot particles being closer to and in physical contact with the reacting surface, it is reasonable to expect that the heat feedback increases in those cases with carbon fibers.

As we mentioned previously, a long-existing challenge in Al-based energetics, especially in aluminized solid propellants, is the exhaust Al$_x$O$_y$ plume that plays a significant role in combustion performance, causing two-phase losses that reduce the specific impulse [57, 59, 110]. Also, as we showed earlier in this chapter, Al nanoparticles start to sinter (agglomerate) when the temperature is near its melting point (933 K), and keep growing (coalescing) into micro-sized spheres on the burning surface [57, 59, 87, 110] until a temperature close to the melting point of Al$_2$O$_3$ (2345 K), when the agglomerations start to detach from the burning surface [59, 87]. The enhanced heat feedback from the inclusion of carbon fibers allows the temperature along the reaction front (red dash lines) to reach as high as ~2400–2600 K (Figure 9.16c), ~400 K higher as compared to the reference case (Figure 9.16a). If the temperature of the reaction front is raised high enough (>2400 K), the small droplets leave the surface early without further coalescing into the droplets, while the references keep coalescing and growing due to their relatively lower temperatures. From these results, one could conjecture that these
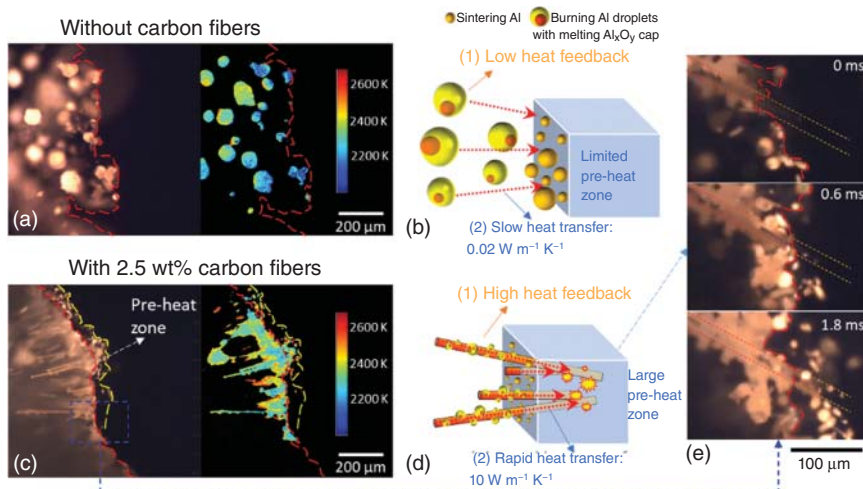
Figure 9.16 Microscopic imaging of Al/CuO composite prints without (a) and with 2.5 wt% (c) carbon fibers; The corresponding cartoons (b and d) illustrate heat feedback to preheat zone; the heated carbon fibers are seen to be inducing the new ignition sites in the preheat zone (e). The propagation is from left to right. Source: Wang et al. [109], Reproduced with permission from American Chemical Society.

embedded carbon fibers can help to reduce the two-phase losses of the aluminized propellants.

9.5.5 Summary

In this section, carbon fibers were embedded into ~90 wt% loading Al/CuO nanothermite sticks that were fabricated via extrusion direct writing. With only ~2.5 wt% carbon fiber addition, the burn rate and heat flux of the sticks were more than doubled. In situ observation on microscopic combustion finds that carbon fibers effectively trap hot agglomerates that could contribute to enhancing heat feedback to the unreacted material. Composite sticks with and without carbon fibers at different equivalence ratios were also investigated, and the results also confirm the enhancement of the carbon fibers on the combustion performance. This study may provide a new means to enhance the propagation and reduce the two-phase flow loss of 3D-printed composite energetics.

9.6 Conclusions and Future Directions

In this chapter, we summarized our recent results on Al/CuO nanothermite composites to show our understanding of how agglomeration affects the energy release rate. Firstly, we developed a universal ink formulation that could bind 90 wt% nanoparticle loading with only 10 wt% polymers for Al/CuO nanothermite composite. The ink rheology and gelation mechanism of ink were studied.

The results show that the shear-thinning and heating-induced-gelation properties make the ink mixture printable. The burn rate, flame temperature, and energy release rate of the printed composites with different equivalence ratios were also investigated. The energy release rate peaks at the equivalence ratio of 1.5–3.5. Secondly, we observed the flame front and agglomeration process of Al/CuO nanothermite composites through an in-operando high spatial (μm) and time (μs) resolution imaging system with pyrometry. We got the correlation between agglomerations and flame front, and the relationship between local agglomerating rate and global propagation rate. Based on the above findings, we demonstrated two typical approaches to engineer the agglomerations and propagations of Al NPs-based high particle loading nanocomposites via the addition of reactive CuO wires and unreactive carbon fibers. In the first approach, by replacing spherical CuO particles with high length-to-diameter CuO wires, we successfully reduced the agglomeration size by three times, evident by our calculations of three times smaller "pocket-size" of Al NPs aggregates reserved by CuO wires. In the other approach, we found 2.5 wt% carbon fiber addition can increase the energy delivery rate by two times. Our further microscopic imaging results reveal that these carbon fibers can effectively trap hot agglomerates, which can enhance heat feedback from the flame front to the unreacted material, thus reducing the agglomerations and promoting the propagations of Al NPs-based composite energetics.

Even though these results and observations offer key insights into agglomeration processes and their relationship to propagation as well as approaches to circumvent some of these limitations. There are still significant gaps in our understanding. For example, previous results about Al agglomeration in Al/CuO nanothermite in late stages include rotating, coalescing, bubbling, and sometimes micro-explosions. However, how the Al agglomerations are formed starting from Al aggregations is unclear. Also, evidence suggests that temperature is one of the key factors that control the micro-explosion of Al agglomerations, but are there other promotion factors that could be applied to enhance the micro-explosions and promote the propagation? Any approaches to turn these factors on and off to alter the energy release rate in situ? Lastly, as our previous studies indicate, coating a gas generator on Al NPs reduces agglomeration in both Al and Al/CuO mesoparticles. But how to make this happen upon adding gas generators into a free-standing energetic composite is an open question. Our current capacity to print high nanothermite particle loading composite and to characterize microscopic combustion in a high spatial and temporal resolution with pyrometry offers a window to study many particle-scale processes occurring in energetic propagation.

References

1 Berthe, J.E., Comet, M., Schnell, F. et al. (2016). Propellants reactivity enhancement with nanothermites. *Propellants, Explosives, Pyrotechnics* 41 (6): 994–998.

2 Comet, M., Martin, C., Klaumünzer, M. et al. (2015). Energetic nanocomposites for detonation initiation in high explosives without primary explosives. *Applied Physics Letters* 107 (24): 243108.

3 Dokhan, A., Price, E.W., Seitzman, J.M., and Sigman, R.K. (2002). The effects of bimodal aluminum with ultrafine aluminum on the burning rates of solid propellants. *Proceedings of the Combustion Institute* 29 (2): 2939–2946.

4 Bocanegra, P.E., Chauveau, C., and Gökalp, I. (2007). Experimental studies on the burning of coated and uncoated micro and nano-sized aluminum particles. *Aerospace Science and Technology* 11 (1): 33–38.

5 Dreizin, E.L. (2009). Metal-based reactive nanomaterials. *Progress in Energy and Combustion Science* 35 (2): 141–167.

6 Yetter, R.A., Risha, G.A., and Son, S.F. (2009). Metal particle combustion and nanotechnology. *Proceedings of the Combustion Institute* 32 (2): 1819–1838.

7 Jian, G., Chowdhury, S., Sullivan, K., and Zachariah, M.R. (2013). Nanothermite reactions: is gas phase oxygen generation from the oxygen carrier an essential prerequisite to ignition? *Combustion and Flame* 160 (2): 432–437.

8 Muthiah, R.M., Krishnamurthy, V.N., and Gupta, B.R. (1992). Rheology of HTPB propellant. I. Effect of solid loading, oxidizer particle size, and aluminum content. *Journal of Applied Polymer Science* 44 (11): 2043–2052.

9 Meda, L., Marra, G., Galfetti, L. et al. (2007). Nano-aluminum as energetic material for rocket propellants. *Materials Science and Engineering: C* 27 (5–8): 1393–1396.

10 Puszynski, J.A., Bulian, C.J., and Swiatkiewicz, J.J. (2007). Processing and ignition characteristics of aluminum-bismuth trioxide nanothermite system. *Journal of Propulsion and Power* 23 (4): 698–706.

11 Sullivan, K., Young, G., and Zachariah, M.R. (2009). Enhanced reactivity of nano-B/Al/CuO MIC's. *Combustion and Flame* 156 (2): 302–309.

12 Armstrong, R.W., Baschung, B., Booth, D.W., and Samirant, M. (2003). Enhanced propellant combustion with nanoparticles. *Nano Letters* 3 (2): 253–255.

13 DeLuca, L.T. (2018). Overview of Al-based nanoenergetic ingredients for solid rocket propulsion. *Defence Technology.* 14 (5): 357–365.

14 McClain, M.S., Gunduz, I.E., and Son, S.F. (2019). Additive manufacturing of ammonium perchlorate composite propellant with high solids loadings. *Proceedings of the Combustion Institute* 37 (3): 3135–3142.

15 Wang, H., Jian, G., Egan, G.C., and Zachariah, M.R. (2014). Assembly and reactive properties of Al/CuO based nanothermite microparticles. *Combustion and Flame* 161 (8): 2203–2208.

16 Wang, H., Jacob, R.J., DeLisio, J.B., and Zachariah, M.R. (2017). Assembly and encapsulation of aluminum NP's within AP/NC matrix and their reactive properties. *Combustion and Flame* 180: 175–183.

17 Teipel, U. and Förter-Barth, U. (2001). Rheology of nano-scale aluminum suspensions. *Propellants, Explosives, Pyrotechnics* 26 (6): 268–272.

18 Kim, S.H. and Zachariah, M.R. (2004). Enhancing the rate of energy release from nanoenergetic materials by electrostatically enhanced assembly. *Advanced Materials* 16 (20): 1821–1825.

19 Severac, F., Alphonse, P., Estève, A. et al. (2012). High-energy Al/CuO nanocomposites obtained by DNA-directed assembly. *Advanced Functional Materials* 22 (2): 323–329.

20 Slocik, J.M., McKenzie, R., Dennis, P.B., and Naik, R.R. (2017). Creation of energetic biothermite inks using ferritin liquid protein. *Nature Communications* 8 (1): 1–7.

21 Bencomo, J.A., Iacono, S.T., and McCollum, J. (2018). 3D printing multifunctional fluorinated nanocomposites: tuning electroactivity, rheology and chemical reactivity. *Journal of Materials Chemistry A* 6 (26): 12308–12315.

22 Murray, A.K., Novotny, W.A., Fleck, T.J. et al. (2018). Selectively-deposited energetic materials: a feasibility study of the piezoelectric inkjet printing of nanothermites. *Additive Manufacturing* 22: 69–74.

23 Sullivan, K.T., Zhu, C., Duoss, E.B. et al. (2016). Controlling material reactivity using architecture. *Advanced Materials* 28 (10): 1934–1939.

24 Comet, M., Martin, C., Schnell, F., and Spitzer, D. (2017). Nanothermite foams: from nanopowder to object. *Chemical Engineering Journal* 316: 807–812.

25 Ghosh, S., Parker, S.T., Wang, X. et al. (2008). Direct-write assembly of microperiodic silk fibroin scaffolds for tissue engineering applications. *Advanced Functional Materials* 18 (13): 1883–1889.

26 Chang, C., Tran, V.H., Wang, J. et al. (2010). Direct-write piezoelectric polymeric nanogenerator with high energy conversion efficiency. *Nano Letters* 10 (2): 726–731.

27 Xu, C., An, C., He, Y. et al. (2018). Direct ink writing of DNTF based composite with high performance. *Propellants, Explosives, Pyrotechnics* 43 (8): 754–758.

28 Ruz-Nuglo, F.D. and Groven, L.J. (2018). 3-D printing and development of fluoropolymer based reactive inks. *Advanced Engineering Materials* 20 (2): 1700390.

29 McDonald, B.A., Rice, J.R., and Kirkham, M.W. (2014). Humidity induced burning rate degradation of an iron oxide catalyzed ammonium perchlorate/HTPB composite propellant. *Combustion and Flame* 161 (1): 363–369.

30 Kurva, R., Gupta, G., Dhabbe, K.I. et al. (2017). Evaluation of 4-(dimethylsilyl) butyl ferrocene grafted HTPB as a burning rate modifier in composite

propellant formulation using bicurative system. *Propellants, Explosives, Pyrotechnics* 42 (4): 401–409.

31 Chandru, R.A., Balasubramanian, N., Oommen, C., and Raghunandan, B.N. (2018). Additive manufacturing of solid rocket propellant grains. *Journal of Propulsion and Power* 34 (4): 1090–1093.

32 Piercey, D.G. and Klapoetke, T.M. (2010). Nanoscale aluminum-metal oxide (thermite) reactions for application in energetic materials. *Central European Journal of Energetic Materials* 7 (2): 115–129.

33 Hastings, D.L., Schoenitz, M., and Dreizin, E.L. (2018). High density reactive composite powders. *Journal of Alloys and Compounds* 735: 1863–1870.

34 Kim, W.D., Lee, S., and Lee, D.C. (2018). Nanothermite of Al nanoparticles and three-dimensionally ordered macroporous CuO: mechanistic insight into oxidation during thermite reaction. *Combustion and Flame* 189: 87–91.

35 Calais, T., Bancaud, A., Estève, A., and Rossi, C. (2018). Correlation between DNA self-assembly kinetics, microstructure, and thermal properties of tunable highly energetic Al–CuO nanocomposites for micropyrotechnic applications. *ACS Applied Nano Materials* 1 (9): 4716–4725.

36 He, W., Liu, P.J., He, G.Q. et al. (2018). Highly reactive metastable intermixed composites (MICs): preparation and characterization. *Advanced Materials* 30 (41): 1706293.

37 Meeks, K., Smith, D.K., Clark, B., and Pantoya, M.L. (2017). Percolation of a metallic binder in energy generating composites. *Journal of Materials Chemistry A* 5 (15): 7200–7209.

38 Weismiller, M.R., Huba, Z.J., Tuttle, S.G. et al. (2017). Combustion characteristics of high energy Ti–Al–B nanopowders in a decane spray flame. *Combustion and Flame* 176: 361–369.

39 Koenig, J.T., Shaw, A.P., Poret, J.C. et al. (2017). Performance of W/MnO$_2$ as an environmentally friendly energetic time delay composition. *ACS Sustainable Chemistry & Engineering* 5 (10): 9477–9484.

40 Martirosyan, K.S. (2011). Nanoenergetic gas-generators: principles and applications. *Journal of Materials Chemistry* 21 (26): 9400–9405.

41 Jian, G., Liu, L., and Zachariah, M.R. (2013). Facile aerosol route to hollow CuO spheres and its superior performance as an oxidizer in nanoenergetic gas generators. *Advanced Functional Materials* 23 (10): 1341–1346.

42 Rossi, C., Estève, A., and Vashishta, P. (2010). Nanoscale energetic materials. *Journal of Physics and Chemistry of Solids* 2 (71): 57–58.

43 Shen, Z., Ding, Y., Chen, J. et al. (2019). Interfacial bonding mechanism in Al/coated steel dissimilar refill friction stir spot welds. *Journal of Materials Science and Technology* 35 (6): 1027–1038.

44 Ali, A.N., Son, S.F., Hiskey, M.A., and Naud, D.L. (2004). Novel high nitrogen propellant use in solid fuel micropropulsion. *Journal of Propulsion and Power* 20 (1): 120–126.

45 Rossi, C., Orieux, S., Larangot, B. et al. (2002). Design, fabrication and modeling of solid propellant microrocket-application to micropropulsion. *Sensors and Actuators A: Physical* 99 (1–2): 125–133.

46 Yen, N.H. and Wang, L.Y. (2012). Reactive metals in explosives. *Propellants, Explosives, Pyrotechnics* 37 (2): 143–155.

47 Sanders, V.E., Asay, B.W., Foley, T.J. et al. (2007). Reaction propagation of four nanoscale energetic composites (Al/MoO$_3$, Al/WO$_3$, Al/CuO, and B$_{12}$O$_3$). *Journal of Propulsion and Power* 23 (4): 707–714.

48 Ilyushin, M.A., Tselinsky, I.V., and Shugalei, I.V. (2012). Environmentally friendly energetic materials for initiation devices. *Central European Journal of Energetic Materials* 9 (4): 293–327.

49 Weismiller, M.R., Malchi, J.Y., Yetter, R.A., and Foley, T.J. (2009). Dependence of flame propagation on pressure and pressurizing gas for an Al/CuO nanoscale thermite. *Proceedings of the Combustion Institute* 32 (2): 1895–1903.

50 Yan, S., Jian, G., and Zachariah, M.R. (2012). Electrospun nanofiber-based thermite textiles and their reactive properties. *ACS Applied Materials and Interfaces* 4 (12): 6432–6435.

51 Baijot, V., Mehdi, D.R., Rossi, C., and Esteve, A. (2017). A multi-phase micro-kinetic model for simulating aluminum based thermite reactions. *Combustion and Flame* 180: 10–19.

52 Chiang, Y.C. and Wu, M.H. (2017). Assembly and reaction characterization of a novel thermite consisting aluminum nanoparticles and CuO nanowires. *Proceedings of the Combustion Institute* 36 (3): 4201–4208.

53 Hübner, J., Klaumünzer, M., Comet, M. et al. (2017). Insights into combustion mechanisms of variable aluminum-based iron oxide/−hydroxide nanothermites. *Combustion and Flame* 184: 186–194.

54 Sullivan, K.T., Kuntz, J.D., and Gash, A.E. (2014). The role of fuel particle size on flame propagation velocity in thermites with a nanoscale oxidizer. *Propellants, Explosives, Pyrotechnics* 39 (3): 407–415.

55 Zohari, N., Keshavarz, M.H., and Seyedsadjadi, S.A. (2013). The advantages and shortcomings of using nano-sized energetic materials. *Central European Journal of Energetic Materials* 10 (1): 135–147.

56 Sullivan, K.T., Piekiel, N.W., Wu, C. et al. (2012). Reactive sintering: an important component in the combustion of nanocomposite thermites. *Combustion and Flame* 159 (1): 2–15.

57 Chakraborty, P. and Zachariah, M.R. (2014). Do nanoenergetic particles remain nano-sized during combustion? *Combustion and Flame* 161 (5): 1408–1416.

58 Ao, W., Liu, X., Rezaiguia, H. et al. (2017). Aluminum agglomeration involving the second mergence of agglomerates on the solid propellants burning surface: experiments and modeling. *Acta Astronautica* 136: 219–229.

59 Chen, Y., Guildenbecher, D.R., Hoffmeister, K.N. et al. (2017). Study of aluminum particle combustion in solid propellant plumes using digital in-line holography and imaging pyrometry. *Combustion and Flame* 182: 225–237.

60 Jin, B.N., Wang, Z.X., Xu, G. et al. (2020). Three-dimensional spatial distributions of agglomerated particles on and near the burning surface of aluminized solid propellant using morphological digital in-line holography. *Aerospace Science and Technology* 106: 106066.

61 Tejasvi, K., Venkateshwara Rao, V., Pydi Setty, Y., and Jayaraman, K. (2020). Ultra-fine aluminium characterization and its agglomeration features in solid propellant combustion for various quenched distance and pressure. *Propellants, Explosives, Pyrotechnics* 45 (5): 714–723.

62 Li, L.B., Chen, X., Zhou, C.S. et al. (2020). Experimental and model investigation on agglomeration of aluminized fuel-rich propellant in solid fuel ramjet. *Combustion and Flame* 219: 437–448.

63 Ao, W., Liu, P., Liu, H. et al. (2020). Tuning the agglomeration and combustion characteristics of aluminized propellants via a new functionalized fluoropolymer. *Chemical Engineering Journal* 382: 122987.

64 Wainwright, E.R., Lakshman, S.V., Leong, A.F. et al. (2019). Viewing internal bubbling and microexplosions in combusting metal particles via x-ray phase contrast imaging. *Combustion and Flame* 199: 194–203.

65 Grapes, M.D., Reeves, R.V., Fezzaa, K. et al. (2019). In situ observations of reacting Al/Fe_2O_3 thermite: relating dynamic particle size to macroscopic burn time. *Combustion and Flame* 201: 252–263.

66 Zong, Y., Jacob, R.J., Li, S., and Zachariah, M.R. (2015). Size resolved high temperature oxidation kinetics of nano-sized titanium and zirconium particles. *The Journal of Physical Chemistry A* 119 (24): 6171–6178.

67 Egan, G.C., Sullivan, K.T., LaGrange, T. et al. (2014). In situ imaging of ultra-fast loss of nanostructure in nanoparticle aggregates. *Journal of Applied Physics* 115 (8): 084903.

68 Zhou, L., Piekiel, N., Chowdhury, S., and Zachariah, M.R. (2009). T-Jump/time-of-flight mass spectrometry for time-resolved analysis of energetic materials. *Rapid Communications in Mass Spectrometry* 23 (1): 194–202.

69 Sullivan, K. and Zachariah, M. (2010). Simultaneous pressure and optical measurements of nanoaluminum thermites: investigating the reaction mechanism. *Journal of Propulsion and Power* 26 (3): 467–472.

70 Wang, H., Julien, B., Kline, D.J. et al. (2020). Probing the reaction zone of nanolaminates at $\sim$ μs time and$\sim$ μm spatial resolution. *The Journal of Physical Chemistry C.* 124 (25): 13679–13687.

71 Wang, H., Shen, J., Kline, D.J. et al. (2019). Direct writing of a 90 wt% particle loading nanothermite. *Advanced Materials* 31 (23): 1806575.

72 Kline, D.J., Alibay, Z., Rehwoldt, M.C. et al. (2020). Experimental observation of the heat transfer mechanisms that drive propagation in additively manufactured energetic materials. *Combustion and Flame* 215: 417–424.

73 Wang, H., Kline, D.J., and Zachariah, M.R. (2019). In-operando high-speed microscopy and thermometry of reaction propagation and sintering in a nanocomposite. *Nature Communications* 10 (1): 1–8.

74 Wang, H., Rehwoldt, M., Kline, D.J. et al. (2019). Comparison study of the ignition and combustion characteristics of directly-written Al/PVDF, Al/Viton and Al/THV composites. *Combustion and Flame* 201: 181–186.

75 Sadasivuni, K.K., Cabibihan, J.J., Ponnamma, D. et al. (ed.) (2016). *Biopolymer Composites in Electronics*. Elsevier.

76 Rae, P.J. and Dattelbaum, D.M. (2004). The properties of poly (tetrafluoroethylene)(PTFE) in compression. *Polymer* 45 (22): 7615–7625.

77 Scott, G.D. and Kilgour, D.M. (1969). The density of random close packing of spheres. *Journal of Physics D: Applied Physics* 2 (6): 863.

78 Zangmeister, C.D., Radney, J.G., Dockery, L.T. et al. (2014). Packing density of rigid aggregates is independent of scale. *Proceedings of the National Academy of Sciences* 111 (25): 9037–9041.

79 Egan, G.C. and Zachariah, M.R. (2015). Commentary on the heat transfer mechanisms controlling propagation in nanothermites. *Combustion and Flame* 162 (7): 2959–2961.

80 Jacob, R.J., Kline, D.J., and Zachariah, M.R. (2018). High speed 2-dimensional temperature measurements of nanothermite composites: probing thermal vs. gas generation effects. *Journal of Applied Physics* 123 (11): 115902.

81 Dutro, G.M., Yetter, R.A., Risha, G.A., and Son, S.F. (2009). The effect of stoichiometry on the combustion behavior of a nanoscale Al/MoO$_3$ thermite. *Proceedings of the Combustion Institute* 32 (2): 1921–1928.

82 Henz, B.J., Hawa, T., and Zachariah, M.R. (2010). On the role of built-in electric fields on the ignition of oxide coated nanoaluminum: ion mobility versus Fickian diffusion. *Journal of Applied Physics* 107 (2): 024901.

83 Povinelli, L.A. and Rosenstein, R.A. (1964). Alumina size distributions from high-pressure composite solid-propellant combustion. *AIAA Journal* 2 (10): 1754–1760.

84 Maggi, F., DeLuca, L.T., and Bandera, A. (2015). Pocket model for aluminum agglomeration based on propellant microstructure. *AIAA Journal* 53 (11): 3395–3403.

85 Cohen, N.S. (1983). A pocket model for aluminum agglomeration in composite propellants. *AIAA Journal* 21 (5): 720–725.

86 Maggi, F., Bandera, A., DeLuca, L.T. et al. (2011). Agglomeration in solid rocket propellants: novel experimental and modeling methods. *Progress in Propulsion Physics* 2: 81–98.

87 Wang, H., Kline, D.J., Biswas, P., and Zachariah, M.R. (2021). Connecting agglomeration and burn rate in a thermite reaction: role of oxidizer morphology. *Combustion and Flame* 231: 111492.

88 Sambamurthi, J.K., Price, E.W., and Sigman, R.K. (1984). Aluminum agglomeration in solid-propellant combustion. *AIAA Journal* 22 (8): 1132–1138.

89 Göçmez, A., Erişken, C., Yilmazer, Ü. et al. (1998). Mechanical and burning properties of highly loaded composite propellants. *Journal of Applied Polymer Science* 67 (8): 1457–1464.

90 Huang, C., Jian, G., DeLisio, J.B. et al. (2015). Electrospray deposition of energetic polymer nanocomposites with high mass particle loadings: a prelude to 3D printing of rocket motors. *Advanced Engineering Materials* 17 (1): 95–101.

91 Shen, J., Wang, H., Kline, D.J. et al. (2020). Combustion of 3D printed 90 wt% loading reinforced nanothermite. *Combustion and Flame* 215: 86–92.

92 Wang, Y., Luo, T., Song, X., and Li, F. (2019). Electrospinning preparation of nc/gap/submicron-hns energetic composite fiber and its properties. *ACS Omega* 4 (10): 14261–14271.

93 Cheng, L., Yang, H., Yang, Y. et al. (2020). Preparation of B/nitrocellulose/Fe particles and their effect on the performance of an ammonium perchlorate propellant. *Combustion and Flame* 211: 456–464.

94 Fehlberg, S., Örnek, M., Manship, T.D., and Son, S.F. (2020). Decomposition of ammonium-perchlorate-encapsulated nanoscale and micron-scale catalyst particles. *Journal of Propulsion and Power* 36 (6): 862–868.

95 Pang, W.Q., DeLuca, L.T., Fan, X.Z. et al. (2020). Combustion behavior of AP/HTPB/Al composite propellant containing hydroborate iron compound. *Combustion and Flame* 220: 157–167.

96 Kubota, N., Ichida, M., and Fujisawa, T. (1982). Combustion processes of propellants with embedded metal wires. *AIAA Journal* 20 (1): 116–121.

97 Isert, S., Lane, C.D., Gunduz, I.E., and Son, S.F. (2017). Tailoring burning rates using reactive wires in composite solid rocket propellants. *Proceedings of the Combustion Institute* 36 (2): 2283–2290.

98 Golobic, A.M., Durban, M.D., Fisher, S.E. et al. (2019). Active mixing of reactive materials for 3D printing. *Advanced Engineering Materials* 21 (8): 1900147.

99 Westphal, E.R., Murray, A.K., McConnell, M.P. et al. (2019). The effects of confinement on the fracturing performance of printed nanothermites. *Propellants, Explosives, Pyrotechnics* 44 (1): 47–54.

100 Wang, H., Biswas, P., Kline, D.J., and Zachariah, M.R. (2022). Flame stand-off effects on propagation of 3D printed 94 wt.% nanosized pyrolants loading composites. *Chemical Engineering Journal* 434: 134487.

101 Rehwoldt, M.C., Kline, D.J., and Zachariah, M.R. (2021). Numerically evaluating energetic composite flame propagation with thermally conductive, high aspect ratio fillers. *Chemical Engineering Science* 229: 116087.

102 Lewicki, J.P., Rodriguez, J.N., Zhu, C. et al. (2017). 3D-printing of meso-structurally ordered carbon fiber/polymer composites with unprecedented orthotropic physical properties. *Scientific Reports* 7 (1): 1–4.

103 Li, N., Li, Y., and Liu, S. (2016). Rapid prototyping of continuous carbon fiber reinforced polylactic acid composites by 3D printing. *Journal of Materials Processing Technology* 238: 218–225.

104 Love, L.J., Kunc, V., Rios, O. et al. (2014). The importance of carbon fiber to polymer additive manufacturing. *Journal of Materials Research* 29 (17): 1893–1898.

105 Tekinalp, H.L., Kunc, V., Velez-Garcia, G.M. et al. (2014). Highly oriented carbon fiber–polymer composites via additive manufacturing. *Composites Science and Technology* 105: 144–150.

106 Yi, Z., Cao, Y., Yuan, J. et al. (2020). Functionalized carbon fibers assembly with Al/Bi2O3: a new strategy for high-reliability ignition. *Chemical Engineering Journal* 389: 124254.

107 Siegert, B., Comet, M., Muller, O. et al. (2010). Reduced-sensitivity nanothermites containing manganese oxide filled carbon nanofibers. *The Journal of Physical Chemistry C.* 114 (46): 19562–19568.

108 Elder, B., Neupane, R., Tokita, E. et al. (2020). Nanomaterial patterning in 3D printing. *Advanced Materials* 32 (17): 1907142.

109 Wang, H., Kline, D.J., Rehwoldt, M.C., and Zachariah, M.R. (2021). Carbon fibers enhance the propagation of high loading nanothermites: in situ observation of microscopic combustion. *ACS Applied Materials and Interfaces* 13 (26): 30504–30511.

110 Karasev, V.V., Onischuk, A.A., Glotov, O.G. et al. (2004). Formation of charged aggregates of Al_2O_3 nanoparticles by combustion of aluminum droplets in air. *Combustion and Flame* 138 (1–2): 40–54.